Physics of Fluids

Numerical study on the hydrodynamic performance of an unconstrained carangiform swimmer

Cite as: Phys. Fluids **34**, 121902 (2022); https://doi.org/10.1063/5.0128635
Submitted: 29 September 2022 • Accepted: 04 November 2022 • Accepted Manuscript Online: 08 November 2022 • Published Online: 06 December 2022

Buchen Wu, Chang Shu, HsuChew Lee, et al.

COLLECTIONS

This paper was selected as Featured

View Online Export Citation CrossMark

ARTICLES YOU MAY BE INTERESTED IN

Understanding the diffusive transport of nanoparticles in agarose hydrogels
Physics of Fluids **34**, 122001 (2022); https://doi.org/10.1063/5.0127687

Fluid force, moment, and torque measurements of oscillating prism and cylinder using loadcell
Physics of Fluids **34**, 127101 (2022); https://doi.org/10.1063/5.0124800

Hydrodynamics of a fish-like body undulation mechanism: Scaling laws and regimes for vortex wake modes
Physics of Fluids **33**, 101904 (2021); https://doi.org/10.1063/5.0062304

Physics of Fluids
Special Topic: Food Physics
Submit Today!

AIP Publishing

© 2022 Author(s).

Physics of Fluids ARTICLE scitation.org/journal/phf

Numerical study on the hydrodynamic performance of an unconstrained carangiform swimmer

Cite as: Phys. Fluids **34**, 121902 (2022); doi: 10.1063/5.0128635
Submitted: 29 September 2022 · Accepted: 4 November 2022 ·
Published Online: 6 December 2022

View Online Export Citation CrossMark

Buchen Wu,[1,2] Chang Shu,[1,a)] HsuChew Lee,[2] and Minping Wan[2,3,4,a)]

AFFILIATIONS

[1]Department of Mechanical Engineering, National University of Singapore, 10 Kent Ridge Crescent, Singapore 119260, Singapore
[2]Guangdong Provincial Key Laboratory of Turbulence Research and Applications, Department of Mechanics and Aerospace Engineering, Southern University of Science and Technology, Shenzhen, Guangdong, 518055, China
[3]Guangdong-Hong Kong-Macao Joint Laboratory for Data-Driven Fluid Mechanics and Engineering Applications, Southern University of Science and Technology, Shenzhen 518055, China
[4]Jiaxing Research Institute, Southern University of Science and Technology, Jiaxing 314031, China

[a)]**Authors to whom correspondence should be addressed:** mpeshuc@nus.edu.sg and wanmp@sustech.edu.cn

ABSTRACT

Undulations are ubiquitous in natural swimmer propulsion, propelling in omni-direction. In the present work, the hydrodynamic performance of an unconstrained carangiform swimmer in the absence of a free stream is numerically investigated at different Reynolds numbers. Propulsive speed is found to increase with an increase in undulatory frequency, wavelength, and Reynolds number. The passive lateral oscillating amplitude is closely related to the wavelength and kinematic viscosity, but insensitive to the undulatory frequency. The propulsive mechanisms for the variation of the propulsive speed are revealed by the vortical structures and the time-averaged velocity field. Scaling relationships are investigated, and we found that the effects of the wavelength on the propulsive performance cannot be neglected at high Reynolds number, i.e., $Re_{ref} \geq 1000$, and the scaling relationship between the flapping Reynolds number and the propulsive Reynolds number is refined with the wavelength adopted as the characteristic length, which generalizes the previous scaling law proposed by Gazzola *et al.* ["Scaling macroscopic aquatic locomotion," Nat. Phys. **10**, 758–761 (2014).] In addition, the scaling relationships related to the power consumption, the cost of transport, the Strouhal number, and the passive lateral oscillating amplitude are revealed. These results are crucial in furthering our understanding of carangiform's self-propulsion and will aid the development of advanced bio-inspired propulsors.

Published under an exclusive license by AIP Publishing. https://doi.org/10.1063/5.0128635

I. INTRODUCTION

Autonomous underwater vehicles (AUVs) have received a considerable amount of attention due to their wide range of applicability, but the propulsive patterns of conventional AUVs have some limitations, such as large power consumption and high forward resistance, especially in complex marine environments. Hence, researchers have focused on a new form of AUVs that are based on swimming and maneuvering capabilities of aquatic animals,[2–7] where they have far superior performances in terms of speed and efficiency than conventional AUVs. Most natural swimmers propel themselves through undulation motion,[6,8–10] which is a wave motion along the swimmers' body, controlling the surrounding flow plastered to its surface. The typical undulatory profiles of natural swimmers are anguilliform, carangiform, subcarangiform, and thunniform,[4,11] and this present work focuses solely on carangiform motion. There are some crucial factors affecting the undulatory motion of a carangiform swimmer, e.g., wavelength, frequency, phase angle, and tail-beat amplitude. The wavelength is an important parameter influencing the hydrodynamic behaviors of the swimmer, and many scientific investigations have been conducted to study its effects on swimming performance. Sfakiotakis *et al.*[11] and Lauder and Madden[12] studied the effect of wavelength on various undulatory profiles and found that the wavelengths of anguilliform swimmers are much shorter than their body's lengths, while the wavelengths of subcarangiform and carangiform swimmers are found to be either equal or slightly larger than the body length. On the other hand, thunniform swimmers adopt wavelengths that are generally greater than their body's lengths, propelling with their caudal fins.

Published under an exclusive license by AIP Publishing

Videler and Wardle[13] revealed that the carangiform swimmer outperforms the anguilliform swimmer in terms of propulsive speed and propulsive efficiency in the inertial regime $Re = \infty$, where the wavelengths of the anguilliform swimmer and the carangiform swimmer are 0.642 and 0.95, respectively. Van Rees *et al.*[14] observed that the optimized geometric shape of an anguilliform swimmer achieves better propulsive performance than natural larval zebrafish, indicating that wave kinematics play a crucial role in helping natural swimmer to propel. Zhang *et al.*[15] investigated the effects of Reynolds number ($50 \leq Re \leq 2 \times 10^5$) and thickness (0.04–0.24) on the propulsive performance of an unconstrained undulatory swimmer, where they showed that the increasing Re resulted in increased propulsive speed and efficiency. However, the propulsive speed enhancement diminishes when $Re > 5 \times 10^4$. In addition, they discovered that thinner foil can achieve a higher propulsive speed and requires less power consumption. Khalid *et al.*[8] investigated the hydrodynamic performance of an anguilliform swimmer and a carangiform swimmer with a wide range of wavelength and undulatory frequency at different Reynolds numbers, where a tethered swimmer model is adopted. They claimed that the production of the thrust force is generally connected to the wake deflection, and the formation of the reverse Bénard-von Kármán (rBvK) vortex configuration is related to the constructive interference between the secondary vortices and the same-signed vortices emerging from opposite sides at the trailing edge. In their subsequent works,[6,9] they studied the effects of wavelength on the propulsive performance of an anguilliform swimmer and a carangiform swimmer in three-dimension configurations, respectively, where the tethered swimmer models are used to study. Their numerical simulations revealed that the wavelengths of 0.65 and 0.80 are suitable for the anguilliform swimmer to achieve better hydrodynamic performance, and longer wavelengths enhance the frictional drag deteriorating its propulsive performance.[6] Meanwhile, the wavelength of 0.8 is beneficial for Jack Fish (a kind of carangiform swimmer) to achieve optimal propulsive efficiency.[9] On the other hand, they also claimed that larger wavelengths enhance the thrust production by the caudal fin and eliminate the drag production on the trunk, requiring less power input. Based on the above reviews, the wavelength and the undulatory frequency are crucial for a natural swimmer's propulsion; hence, the influences introduced by these two parameters on the carangiform swimmer's self-propulsion are investigated in the present work.

Although the interactions between undulatory motions and propulsive performance are complex, many researchers attempt to derive some simple correlation laws behind the propulsion.[1,16–25] Gazzola *et al.*[1] derived a scaling law between the dimensionless swimming number and the propulsive Reynolds number, which links the cruising speeds, the bio-propulsive parameters, and the fluid characteristics. Yu and Huang[24] uncovered a scaling relationship for predicting the hydrodynamic thrust generated by the wave motion, indicating that the thrust generation depends on the Struhal number *St*, the relative speed of wave motion, and forward cruising speed.

In nature, the carangiform swimmer can freely propel in omnidirection, but most studies that are available in the literature placed their focus on the tethered swimmer, constraining it at a fixed position. Moreover, to the best of the authors' knowledge, the investigations on the wavelength and undulatory frequency of an unconstrained carangiform swimmer at different Reynolds numbers remain sparse. In the present work, the hydrodynamic performances of an unconstrained carangiform swimmer are systematically studied to unravel how carangiform swimmer's hydrodynamic performance varies under different kinematic parameters and find some simple scaling laws behind the self-propulsion. In Sec. II, the problem description and methodology are described. Numerical validations and grid-time independence studies are provided in Sec. III. Numerical results and discussions are described in Sec. IV followed by conclusions in Sec. V.

II. PROBLEM DESCRIPTION AND MATHEMATICAL FORMULATION

The NACA 0012 foil is adopted in this study to simulate the shape of a carangiform swimmer, and the backbone undulation of this swimmer is mimicked with a prescribed undulatory motion. The amplitude profile $A(x^*)$ of the carangiform swimmer can be written as follows:

$$A(x^*) = C_0 - C_1 x^* + C_2 (x^*)^2, \quad x^* \in [0, L], \tag{1}$$

where x^* is the local coordinate along the swimmer's body; L denotes the swimmer's body length; C_0, C_1, and C_2 are the propulsive coefficients of a steadily swimming saithe fish and they are specified as 0.02, 0.0825, and 0.1625, respectively in this study. The backbone motion is determined by the undulatory governing equation as follows:

$$y^*(x^*, t) = A(x^*) \cos(kx^* - 2\pi f^* t), \tag{2}$$

where $k = 2\pi/\lambda^*$ is the wave number, λ^* is the wavelength, f^* is the undulatory frequency, and y^* denotes the local lateral displacement of the backbone. Here, the dimensionless wavelength ($\lambda = \lambda^*/L$) is introduced to characterize the wavelength and the non-dimensional undulatory frequency is defined as $f = f^* L/U_{ref}$. Figure 1 shows the schematic view of a carangiform swimmer self-propelling in the computational domain. The Neumann boundary conditions ($\partial \mathbf{u}/\partial n = 0$) are being applied on four domain boundaries, and the propulsive region is discretized by uniform cartesian mesh. Moreover, the locomotion of the carangiform swimmer is governed by Newton's second law as follows:

$$M \frac{d^2 \mathbf{\Psi}}{dt^2} = \boldsymbol{F_H}, \tag{3}$$

where $\mathbf{\Psi}$ denotes the position of the mass center in both horizontal and vertical directions and $\boldsymbol{F_H}$ is the hydrodynamic force applied on the swimmer surface by surrounding flows. $M = \rho_s S$ is the mass of the carangiform swimmer, where ρ_s is the area density of the swimmer

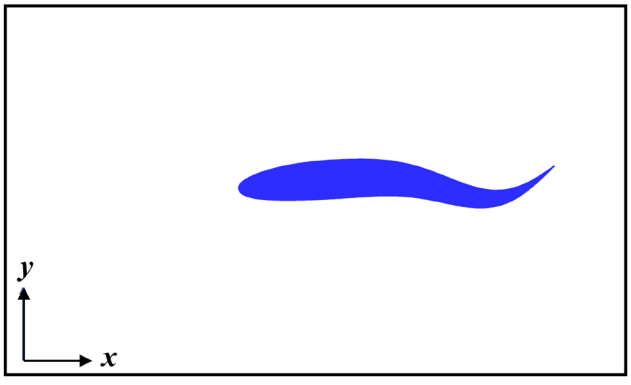

FIG. 1. Schematic view of the simplified carangiform swimmer model.

Published under an exclusive license by AIP Publishing

and S is the area of the swimmer. The value of $S = 0.086\,21\ \mathrm{m}^2$ from Zhang *et al.*[15] is adopted in this work. Since the mass ratio is not the focus of the present work, the area density of the foil is specified such that it is identical to the fluid density. The time-averaged horizontal and lateral propulsive speeds are computed to quantify the hydrodynamic performance of the swimmer as follows:

$$u_x = -\frac{1}{T}\int_0^T u_{xi}dt, \quad u_y = \frac{1}{T}\int_0^T u_{yi}dt, \tag{4}$$

where u_{xi} and u_{yi} denote the instantaneous propulsive speed along the horizontal and lateral directions, respectively. The instantaneous power consumption for generating the wave oscillation of the swimmer can be expressed as follows:

$$P_i = -\oint_s f_{sy}u_{sy}ds, \tag{5}$$

where f_{sy} and u_{sy} denote the instantaneous lateral hydrodynamic force and lateral oscillating speed per unit length on the swimmer surface, respectively. Note that the hydrodynamic forces are evaluated by the velocity corrections in immersed boundary method. The time-averaged power consumption is defined as $P = \frac{1}{T}\int_0^T P_i dt$. To evaluate the propulsive efficiency of the carangiform swimmer, the propulsive efficiency is defined as the ratio of the time-averaged kinetic energy ($E_k = \frac{1}{2}mu_x^2$) to the averaged input work ($W = PT$), namely, $\eta = E_k/W$. In addition, the cost of transport (CoT) is another important quantity to evaluate the power consumption for swimming per unit distance with a per unit mass. The CoT can be expressed as follows:

$$\mathrm{CoT} = \frac{P}{mu_x}. \tag{6}$$

For incompressible flow, the Navier–Stokes (NS) equations of mass and momentum conservation can be written as follows:

$$\nabla \cdot \mathbf{u} = 0, \tag{7a}$$

$$\frac{\partial \mathbf{u}}{\partial t} + \mathbf{u}\cdot\nabla\mathbf{u} = -\frac{1}{\rho}\nabla p + \nu\cdot\nabla^2\mathbf{u} + \mathbf{f}, \tag{7b}$$

where ρ is the fluid density, $\mathbf{u}$ denotes the flow velocity, ν is the kinematic viscosity, p is the pressure, and $\mathbf{f}$ is the force exerted by the solid system on the fluid. The reference Reynolds number is defined as $Re_{ref} = U_{ref}L/\nu$, where U_{ref} denotes the reference velocity.

It is worth mentioning here that we understand that the flow field around a realistic swimmer is essentially three dimensional induced by high propulsive speed and the complexity of the fin's geometry. In addition, recent experiments[26–28] and numerical studies[6,9,29] have investigated the propulsive mechanism behind the natural swimmer propulsion under a three-dimensional setting. However, most of the 3D numerical simulation works focused on tethered swimmer models which requires significantly less computational power than 3D numerical simulation of untethered swimmer models. Therefore, this study adopted a 2D model to investigate the hydrodynamic performance. The simulated flow field conducted in this work can be viewed as a slice cutting through the mid-planes of a realistic swimmer with infinite length along the spanwise direction. Moreover, several previous studies[30–32] have compared the results obtained under 2D and 3D setup to be minimal and the mechanisms uncovered through a 2D swimmer model remained valid under 3D setting.

TABLE I. The specific values of the governing parameters applied in current simulations.

Parameters	Specifications
Re_{ref}	100, 1000, 5000
Wavelength λ	0.5, 0.75, 1.0, 1.25, 1.5
Frequency f	0.5, 1.0, 1.5, 2.0, 2.5, 3.0
Tail-beat amplitude A	0.1

The governing dimensionless parameters used in this study are tabulated in Table I. The Reynolds numbers are varied from 100 to 5000 to systematically investigate the propulsive behavior of the carangiform swimmer. The selected wavelengths in this study are based on the dataset[4,11] of many natural swimmers to better understand the propulsive behavior of different aquatic species. Note that celerity is crucial for the self-propulsion of realistic swimmers, although the internal relationship between the frequency and wavelength is not the focus of the present work.

III. NUMERICAL VALIDATION AND INDEPENDENCE STUDY

The incompressible viscous flows are simulated using the reconstructed lattice Boltzmann flux solver (RLBFS),[33] which is a weakly compressible flow solver and has been widely adopted to simulate incompressible viscous flow. The fluid–structure interaction process is achieved through the explicit boundary condition-enforced immersed boundary method[34] with no slip boundary conditions being applied on the surface of the swimmer. Readers are referred to our previous works[33–36] for more information regarding the numerical methods employed in this work.

To validate our numerical simulation method, two cases related to a single carangiform swimmer have been tested: a stationary case and a self-propelled case. Figure 2(a) shows that the present results of the lift and drag force coefficient of the tethered wave foil are in good agreement with the work of Dong and Lu.[37] Figure 2(b) presents the time history of the horizontal speed of a self-propelled undulatory swimmer. While there are some obvious discrepancies between different numerical methods used in the present work and also previous works, all numerical methods approach a similar value of -1.23 after the swimmer achieves steady propulsion and the time-averaged horizontal speed obtained in this study is consistent with previous studies.[34,38]

Grid and time independence studies are conducted to determine the appropriate grid spacing and time step. Figure 3 shows the hydrodynamic performance of the carangiform swimmer, including the horizontal propulsive speed u_{xi}, the lateral propulsive speed u_{yi}, and the power coefficient P_i, for different grids and time steps. It is evident from Fig. 3 that the spatial resolution of $\Delta x = 0.0033$ and the time step of $\Delta t = 3 \times 10^{-5}$ are sufficient to investigate the hydrodynamic performance of the swimmer with appropriate computational cost and accuracy.

IV. RESULTS AND DISCUSSION

A. Effects of undulatory frequency and wavelength

In this section, the effects of undulatory frequency f and wavelength λ on the propulsive performance of the carangiform swimmer are explored at $Re_{ref} = 1000$.

Published under an exclusive license by AIP Publishing

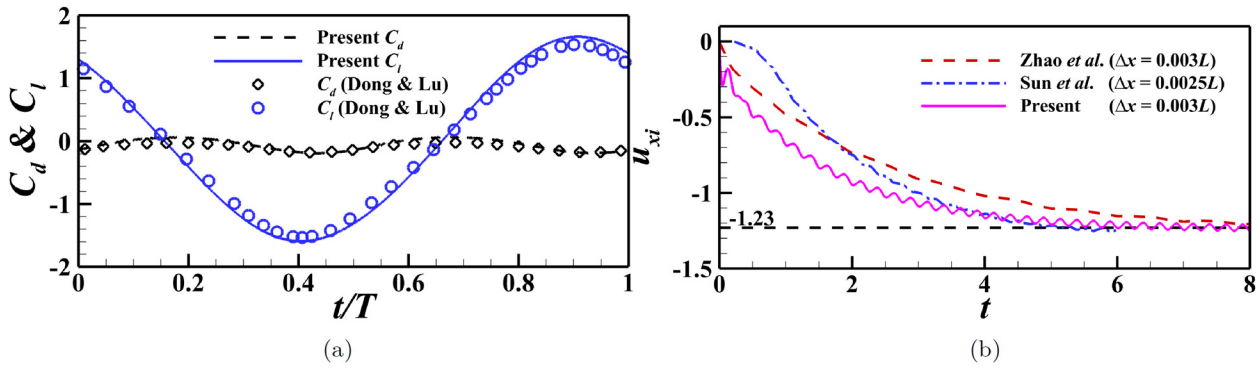

FIG. 2. (a) The lift and drag coefficient of the tethered wave foil at $Re_{ref} = 5000$, $\lambda = 1$, $f = 2$; (b) the horizontal propulsive speed of the carangiform swimmer at $Re_{ref} = 5000$, $\lambda = 1$, $f = 2$.

1. Propulsive performances

Figure 4 shows the time-averaged horizontal propulsive speed (u_x), power consumption (P), and cost of transport (CoT) at different undulatory frequencies and wavelengths. It is evident from Fig. 4(a) that u_x increases with the increase in both undulatory frequency and wavelength. Similarly, P and CoT show the same variation trend as that observed in Fig. 4(a). In contrast to tethered wave foil in the uniform flow in which wave foil only generates thrust at specific conditions,[8] present simulations reveal that the carangiform swimmer can propel forward in all cases considered in this study in the absence of free stream flow, consistent with the findings of Zhang *et al.*[15]

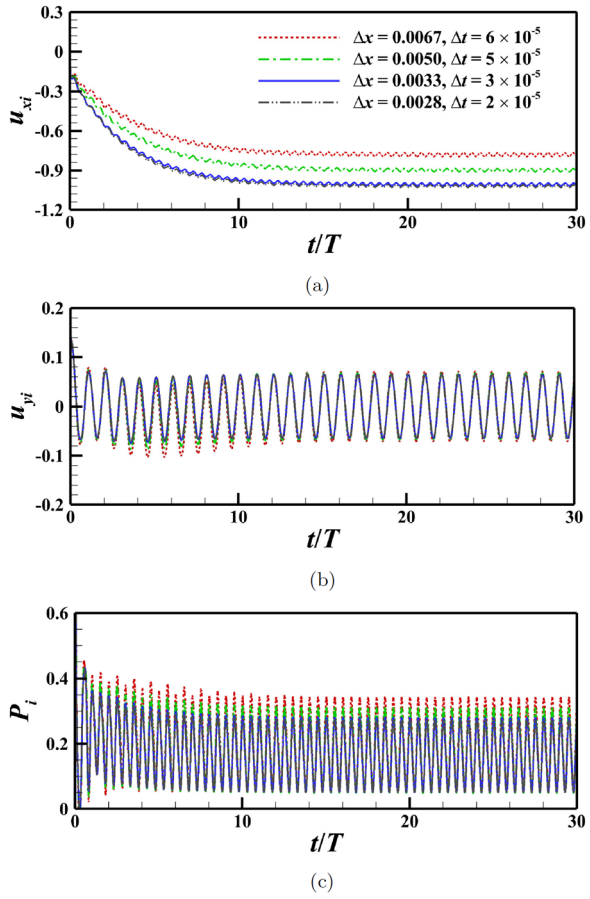

FIG. 3. Grid and time independence studies: time histories of (a) horizontal propulsive speed, (b) lateral propulsive speed, and (c) power consumption. The parameters of $Re_{ref} = 5000$, $\lambda = 1$, and $f = 2$ are adopted.

Compared with the u_x, the time-averaged lateral propulsive speed u_y in all investigated cases is found to be $O(10^{-4})$, where it can be regarded negligible. Hence, the vertical oscillation amplitude A_y is further examined to investigate the vertical propulsive performance, as depicted in Fig. 4(d). It clearly shows that the vertical oscillation amplitude A_y of the mass center is relatively low in all cases, indicating that the unconstrained carangiform swimmer can propel along the horizontal direction with negligible vertical oscillations. In addition, the A_y increases with the λ, but is insensitive to the undulatory frequency f. Interestingly, the vertical oscillating amplitude is smaller than other investigated cases when the wavelength $\lambda = 0.5$. Therefore, small wavelength and large undulatory frequency are beneficial for the unconstrained carangiform swimmer to reduce the redundant mass center's vertical oscillation, which may provide some optimal strategies for AUV designs to stabilize the mass center's vertical oscillation.

To further evaluate the efficiency of the carangiform swimmer, Fig. 5 shows the propulsive efficiency with various parameters at $Re_{ref} = 1000$. It is evident from Fig. 5 that the propulsive efficiency η increases with the increase in the undulatory frequency, while there is an optimal range of $\lambda \in [0.75, 1]$ for the swimmer to achieve relative high propulsive efficiency, and outside the optimal range of λ would reduce the propulsive efficiency. Khalid *et al.*[9] also reported that the carangiform swimmer could achieve the highest propulsive efficiency when $\lambda = 0.8$ from the 3D simulations with a realistic swimmer model of Jack Fish.

2. Wake vortex structure

The wake vortical structures and the time-averaged velocity field around the carangiform swimmer are examined to further analyze the mechanisms behind the hydrodynamic behaviors. Figure 6 shows the instantaneous vortical structures of three cases with different propulsive parameters. As shown in Fig. 6, the reverse Bénard-von Kármán

Published under an exclusive license by AIP Publishing

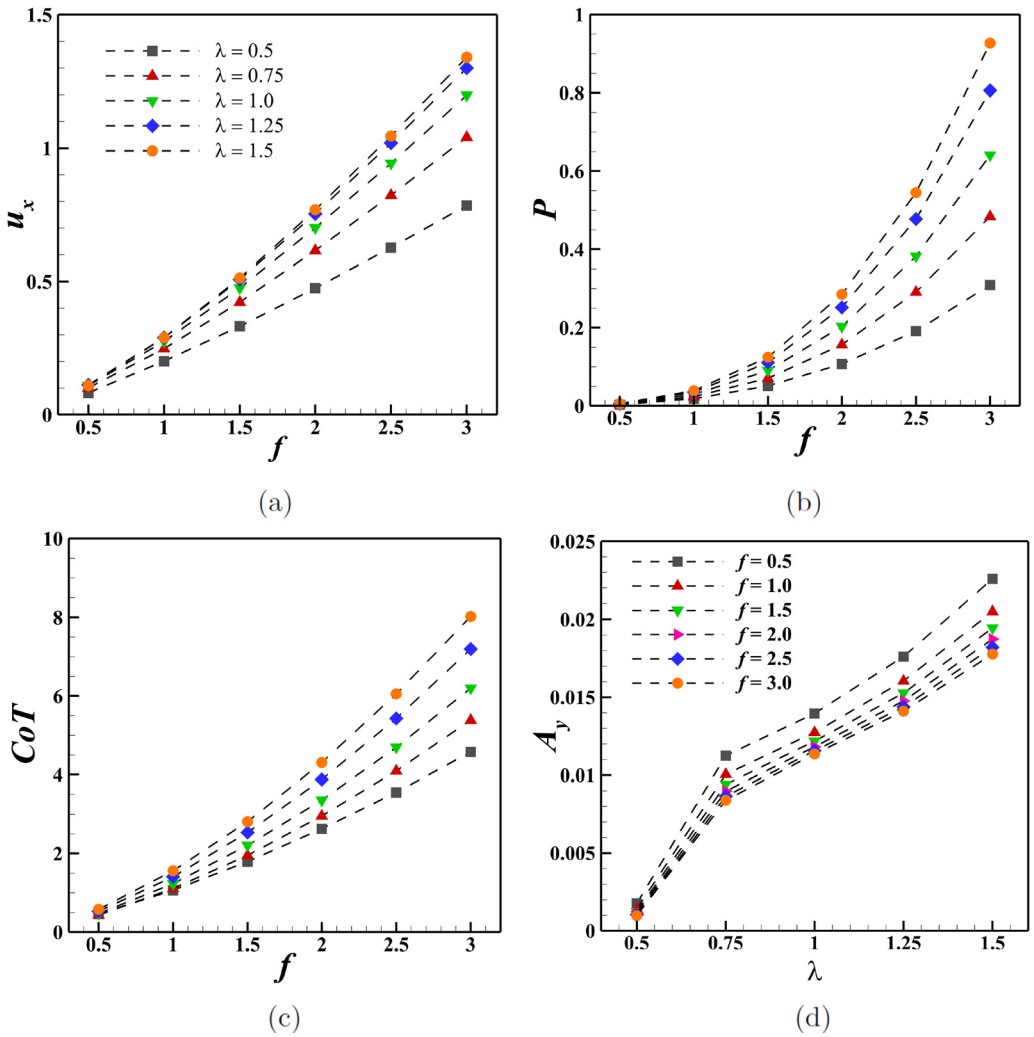

FIG. 4. (a) The time-averaged horizontal propulsive speed u_x, (b) power consumption P, (c) cost of transport CoT, and (d) vertical passive oscillation amplitude A_y of the caranginiform swimmer at $Re_{ref} = 1000$ with different wavelengths and undulatory frequencies.

(rBvK) vortex street is formed in the wake flow, and the vortex generation pattern varies with the wavelength λ and the undulatory frequency f. Based on the undulatory governing equation [Eq. (2)], the lateral oscillating velocity at the trailing edge can be expressed as follows:

$$\left.\frac{\partial y^*}{\partial t}\right|_{x^*=L} = -2\pi f^* A(L)\sin(kx^* - 2\pi f^* t). \tag{8}$$

From Eq. (8), the amplitude of the tail-beat velocity is only related to the undulatory frequency; therefore, the amplitudes of the tail-beat velocity in cases 1 and 2 are the same. However, as shown in Figs. 6(a) and 6(b), increasing the wavelength λ promotes the vortical strength of the shedding vortices and ambient fluid can provide a large reactive thrust force to the swimmer following Newton's third law. The reason for the large vortical strength in case 2 is that the large wavelength allows the bound vortex amalgamation in a long region before reaching the inflection point, promoting the vortical strength of the shedding bound vortex. The secondary vortices are also observed in Fig. 6(a) near the inflection point, which breaks up the amalgamation of the same-signed vortices on each side. From Figs. 6(b) and 6(c), high undulatory frequency further promotes the strength of the wake vortices, because increasing undulatory frequency strengthens the amplitude of tail-beat velocity.

Figure 7 shows the time-averaged horizontal velocity fields of these cases to evaluate the correlation relationship between the vortical strength and the propulsive speed. As shown in Fig. 7, a jet wake flow is formed by the rBvK configurations, providing the reactive thrust force for the swimmer. The velocity profiles along the lateral direction behind the swimmer are shown in Fig. 7(d), and it shows that the strength of the wake jet highly correlates with the propulsive speed, which is consistent with the previous works.[39,40] Due to the tail-beat amplitude being constant, the wake width is maintained.

Published under an exclusive license by AIP Publishing

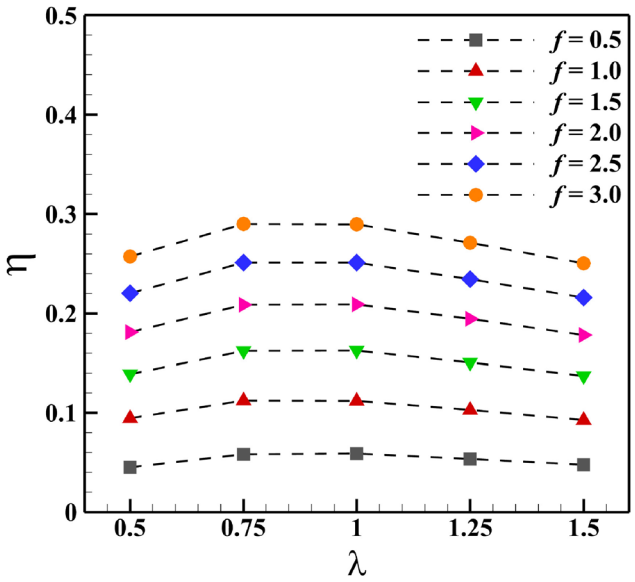

FIG. 5. The propulsive efficiency of the carangiform swimmer at $Re_{ref} = 1000$ with different propulsive parameters.

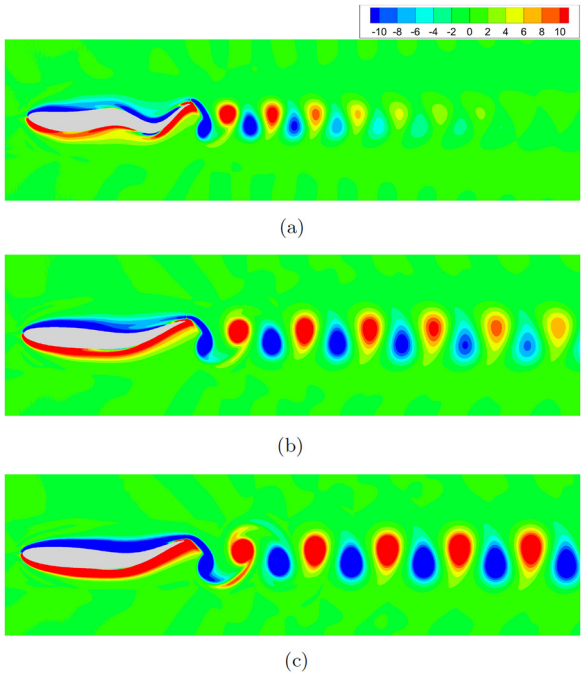

FIG. 6. The instantaneous vortical structures of the carangiform swimmer with (a) case 1: $\lambda = 0.5, f = 2$; (b) case 2: $\lambda = 1, f = 2$; and (c) case 3: $\lambda = 1, f = 3$ at $Re_{ref} = 1000$ when $t = T$.

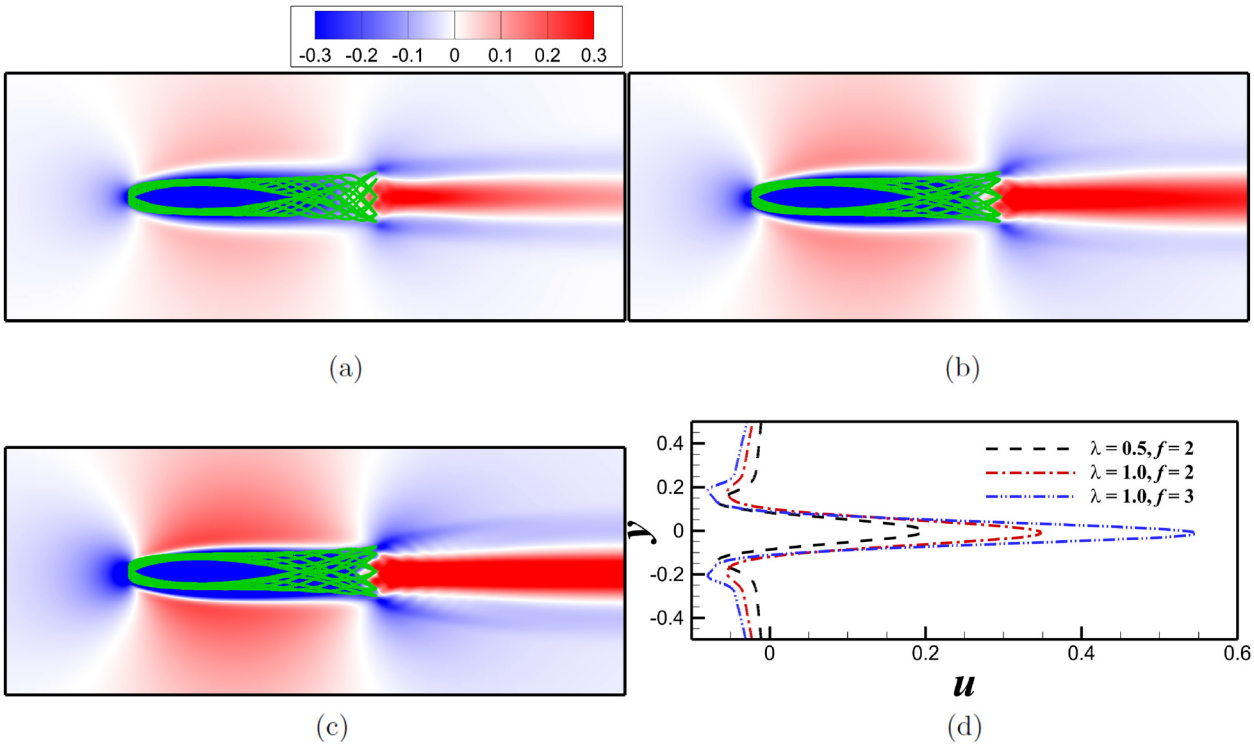

FIG. 7. The time-averaged horizontal velocity fields of (a) case 1, (b) case 2, and (c) case 3. (d) The velocity profile of these three cases at $x/L = 1.5$.

Published under an exclusive license by AIP Publishing

B. Effects of Reynolds number

In this section, the effects introduced by the Reynolds number are analyzed. The parameters of $\lambda = 0.75$ and 1.25 are adopted, and the undulatory frequency f changes from 0.5 to 3 with an interval of 0.5.

1. Propulsive performance

The time-averaged horizontal propulsive speed u_x, power consumption P, cost of transport CoT, mass center's vertical oscillating amplitude A_y, and propulsive efficiency η are shown in Fig. 8. It shows that at a fixed undulatory frequency, the swimmer can achieve a higher propulsive speed at high Re_{ref} [see Fig. 8(a)], because the kinematic viscosity ν decreases with an increase in Re_{ref}; thus, the viscous forces applied on the swimmer's surface is reduced in high Re_{ref} environment. Due to the larger viscous forces on the swimmer at low *Reref*, the self-propulsion requires more power consumption; hence, the P decreases as Re_{ref} increases. On the other hand, Eq. (6) indicates that the CoT is only related to the power consumption and the propulsive speed. Hence, the increase in Re_{ref} causes large propulsive speed and low power consumption, which in turn leads to a decrease in CoT and an increase in propulsive efficiency, echoing the observations reported in previous studies.[15,41] The propulsive efficiency η shows a similar trend at different Reynolds numbers; the η is highly correlated with the undulatory frequency and shows small variations with different wavelengths. The A_y is also insensitive to the undulatory frequency at different Re_{ref} and A_y is reduced at high Re_{ref}. The reason might be because the high horizontal propulsive speed obtained at high Re_{ref} stabilizes the mass center's lateral oscillation. Furthermore, the decrease in viscous force attenuates the fluctuation of the lateral hydrodynamic force, thereby, effectively reduces A_y.

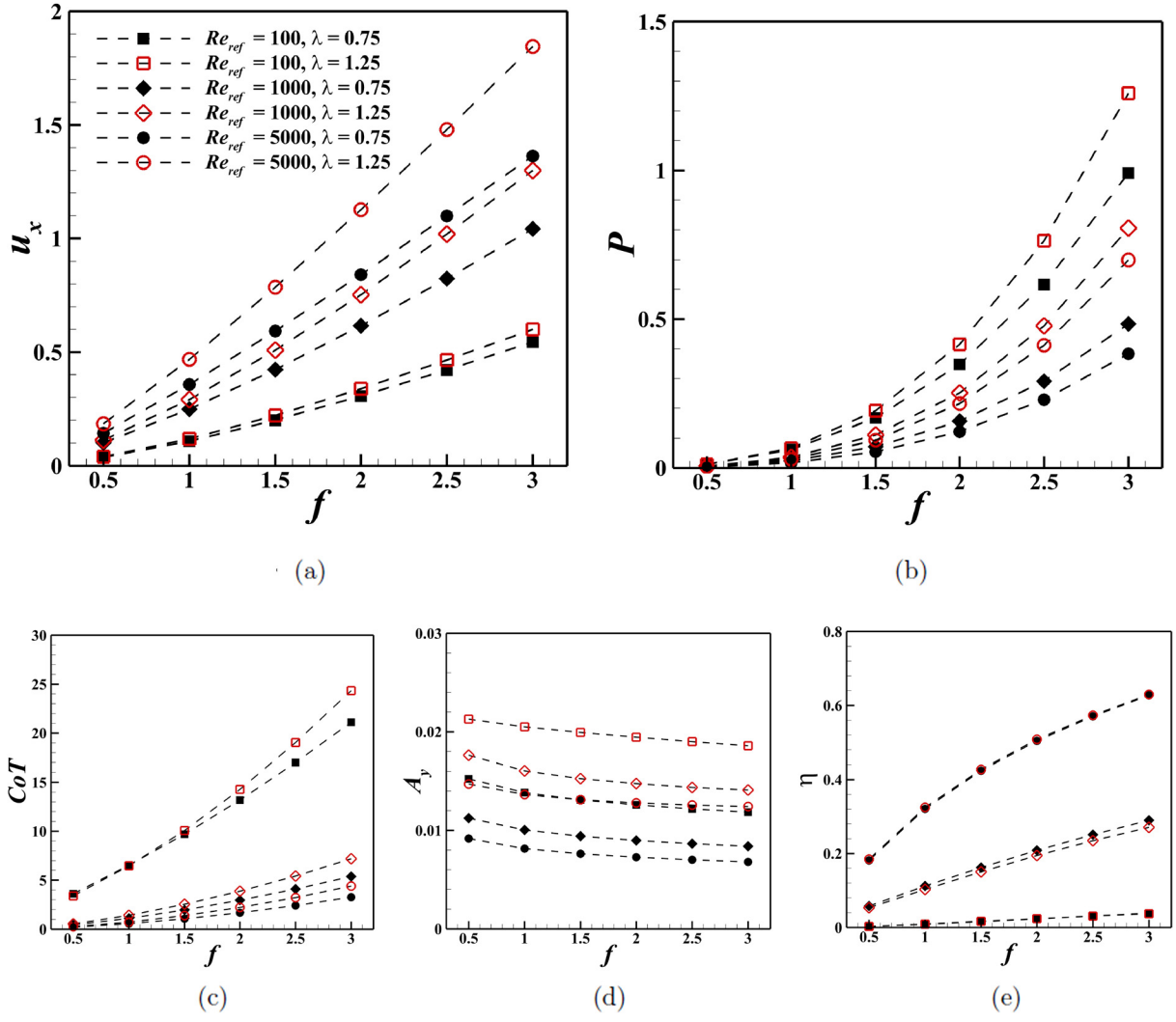

FIG. 8. (a) The time-averaged horizontal propulsive speed u_x, (b) power consumption P, (c) cost of transport CoT, (d) vertical passive oscillation amplitude A_y, and (e) propulsive efficiency η of the carangiform swimmer at different Reynolds numbers.

Published under an exclusive license by AIP Publishing

2. Wake vortex structure

The propulsive performances of the carangiform swimmer are closely related to the wake flow structure; thus, the vortical structures around the swimmer are explored to investigate the influences introduced by the Re_{ref}. It is evident from Fig. 9 that the wake vortex configurations are tightly related to the Reynolds number Re_{ref}. At $Re_{ref} = 100$, the leading-edge vortex (LEV) is formed in the anterior body due to the separation of the boundary layer. Subsequently, the LEV is transported to the posterior body through the swimmer body's wave motion and finally being shed downstream. The shedding vortices vanish rapidly due to the high kinematic viscosity. At $Re_{ref} = 1000$, the reverse Bénard-von Kármán (rBvK) configurations are formed by the shedding vortex from the trailing edge, and the formation of the 2S-type rBvK is closely related to the generation of the reactive thrust force. It should be noted that the bound vortices envelop the swimmer and can be amalgamated on the surface to enhance the strength of the shedding vortices. As Re_{ref} increases to 5000, the boundary layers around the swimmer's surface become thinner. As shown in Fig. 9, the effects of Reynolds number can be concluded as follows: with the increase in Re_{ref}, the kinematic viscosity ν decreases, and thus the horizontal propulsive speed is enhanced. In previous studies, the Strouhal number ($St = f^* A_{max}/u_x$) is a significant dimensionless frequency in bio-locomotion studies, which evaluates the ratio of wake width to the streamwise spacing of the shedding vortices. As the horizontal speed increases, the Strouhal number decreases, triggering that the wake wavelength increases with a longer streamwise spacing of the shedding vortices.

As described in Sec. IV A 2, the wake vortex street is highly related to the jet wake flow shown in the time-averaged velocity field.

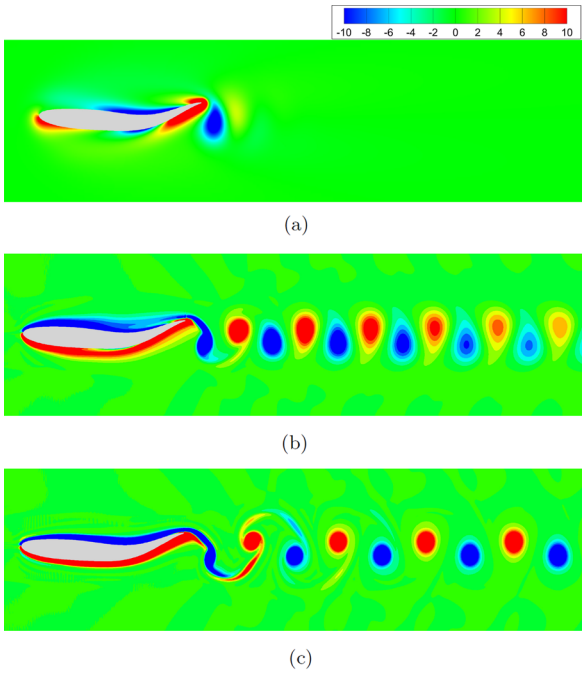

FIG. 9. The instantaneous vortical structures around the carangiform swimmer with $\lambda = 1, f = 2$ at (a) $Re_{ref} = 100$, (b) $Re_{ref} = 1000$, and (c) $Re_{ref} = 5000$ when $t = T$.

The time-averaged velocity field corresponding to the wake vortical structures from Fig. 9 are presented in Fig. 10. As shown in Fig. 10, the characteristics of the time-averaged velocity field vary significantly at different Reynolds numbers. The most notable differences induced by the Reynolds number effects can be summarized as follows: at $Re_{ref} = 100$, the boundary layer around the swimmer is dragged to induce forward motion, and the wake jet flow diminishes rapidly due to the significant viscous dissipation effect; on the other hand, at $Re_{ref} = 1000$ and 5000, the boundary layers are much thinner and the strength of wake jets are more robust than those at $Re_{ref} = 100$. The velocity profiles [see Fig. 10(d)] indicate that the reactive thrust force is correlated with the strength of the jet flow. Although the strengths of the wake jet in the cases at $Re_{ref} = 1000$ and 5000 are close, the viscous forces applied on the swimmer's surface are relatively small at $Re_{ref} = 5000$, resulting in a high propulsive speed.

C. Scaling laws

While the general physical characteristics of the propulsive behaviors of the carangiform swimmer are examined in Secs. IV A and IV B at various Reynolds numbers, the existences of some universal physical laws behind these phenomena requires further investigation. In previous studies,[1,42] the propulsive mechanism is closely related to the flapping Reynolds number and the propulsive Reynolds number. Hence, the relationship between the flapping Reynolds number ($Re_f = f^* A_{max} L_{ref}/\nu$, where $A_{max} = 2A$) and the propulsive Reynolds number ($Re_u = u_x L_{ref}/\nu$) is analyzed, as shown in Fig. 11. Previous studies[19,43–45] have shown that, for traveling wave plate, the wavelength is crucial for scaling the propulsive quantities and is used to represent the characteristic length to non-dimensionalize lengths. With this consideration, two different characteristic length scales L_{ref} are examined by replacing the L_{ref} with the swimmer's body length (following the scaling law proposed by Gazzola *et al.*[1]) in Fig. 11(a) and with the wavelength in Fig. 11(b). The numerical data shown in Fig. 11(a) deviate from the fitting line at high flapping Reynolds number, and the deviation increases with increasing flapping Reynolds number, indicating that the effects of wavelength on the propulsive performance cannot be neglected at high Reynolds number, i.e., $Re_{ref} > 1000$. On the other hand, the numerical data shown in Fig. 11(b) collapse onto the fitting line even at high Reynolds number conditions when the wavelength is adopted as the characteristic length scale in the Reynolds numbers. From the results of regression analysis, Fig. 11 shows that the relationship between Re_u and Re_f is highly linear with correlation coefficient $R^2 > 0.99$, and most importantly, the sum of squares regression (SSR) indicates that the distribution obtained using the wavelength is more consistent with the regression model.

To generalize the previous scaling law[1] which cannot satisfy the influence introduced by the wavelength, the scaling relationship between the flapping Reynolds number and the propulsive Reynolds number is improved. The thrust generation is related to the trailing edge flapping acceleration $\partial^2 y^*/\partial t^2 = -A(2\pi f^*)^2 \cos(k - 2\pi f^* t) \sim Af^{*2}$, the mass of fluid per unit depth $\rho L^2 = \rho(\lambda^*/\lambda)^2 \sim \rho\lambda^{*2}$, and the local angle $\theta = \partial y^*/\partial x^* = -Ak \sin(k - 2\pi f^* t) \sim Ak = A \cdot 2\pi/\lambda^* \sim A\lambda^{*-1}$. Hence, the thrust force scale can be expressed as $Af^{*2} \cdot \rho\lambda^{*2} \cdot A\lambda^{*-1} = \rho A^2 f^{*2} \lambda^*$. The skin viscous drag per unit depth scale can expressed as $\mu u_x L/\delta = \mu u_x \lambda^*/\delta\lambda \sim \mu u_x \lambda^*/\delta$. With the scale relationship $\delta \sim Re^{-1/2}$ obtained through classical Blasius theory for fast laminar flows, the drag force scale can be written as

Published under an exclusive license by AIP Publishing

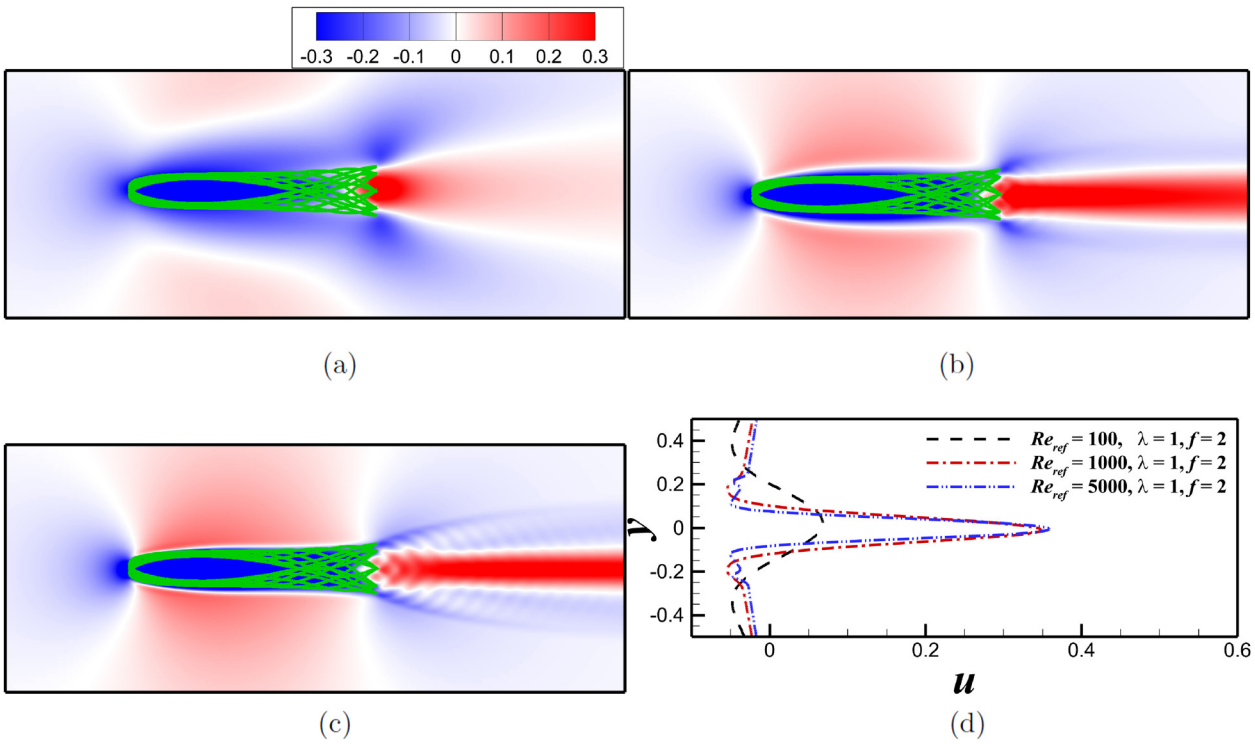

FIG. 10. The time-averaged horizontal velocity fields around the carangiform swimmer with $\lambda^* = 1, f^* = 2$ at (a) $Re_{ref} = 100$, (b) $Re_{ref} = 1000$, and (c) $Re_{ref} = 5000$. (d) The velocity profile of these three cases at $x/L = 1.5$.

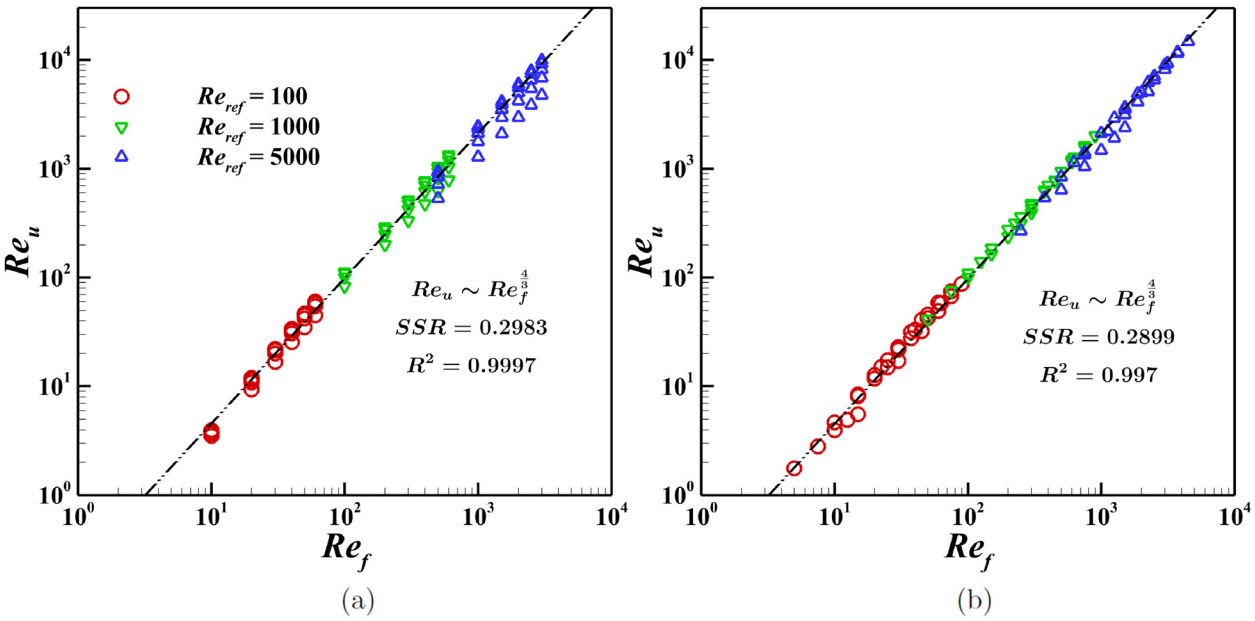

FIG. 11. The relationship between the propulsive Reynolds number and the flapping Reynolds number, and characteristic length adopts (a) the swimmer's body length L and (b) the swimmer's wavelength λ.

Published under an exclusive license by AIP Publishing

$\mu u_x \lambda^* / Re^{-1/2} \sim \rho(\nu\lambda^*)^{-1/2} {u_x}^{3/2}$. At steady propulsive stage, the balance between the thrust force and the drag force is achieved, which yields $\rho(\nu\lambda^*)^{-1/2} {u_x}^{3/2} = \rho A^2 f^{*2} \lambda^*$, hence, $u_x \sim A^{4/3} f^{*4/3} \lambda^{*1/3} \nu^{-1/3}$, and this relationship can be rewritten as follows:

$$\frac{u_x \lambda^*}{\nu} \sim \left(\frac{Af^*\lambda^*}{\nu}\right)^{4/3}, \tag{9a}$$

$$Re_u \sim Re_f^{4/3}. \tag{9b}$$

The above scaling law is consistent with the correlation relationship found in Fig. 11, which demonstrates that the wavelength may be more suitable for representing the character length scale. Note that the scaling law of Eq. (9b) is applicable only when the boundary layer around the swimmer is laminar. This is when the boundary layer transits from laminar to turbulent at high Reynolds numbers, the viscous force becomes negligible, and the force balance is the thrust force and the pressure drag.

As previously described, high propulsive speed u_x generally requires more power consumption P. However, there is no obvious relationship between these two quantities. Surprisingly, the scale relationship between u_x and P in log–log scale can be approximately expressed as $P \sim u_x^2$, as shown in Fig. 12(a). Moreover, the relationship between CoT and u_x can be described as CoT $\sim u_x$ [see Fig. 12(b)]. It can be observed that these scaling relationships can describe the hydrodynamic behaviors at different Reynolds numbers, which may be useful to evaluate the power consumption and CoT at different propulsive speeds.

Figure 12(c) shows the scaling relationship between the St and the propulsive Reynolds number Re_u based on the wavelength, which can be approximately expressed as $St \sim Re_u^{-1/4}$, consistent with the physics law revealed by Gazzola *et al.*[1]

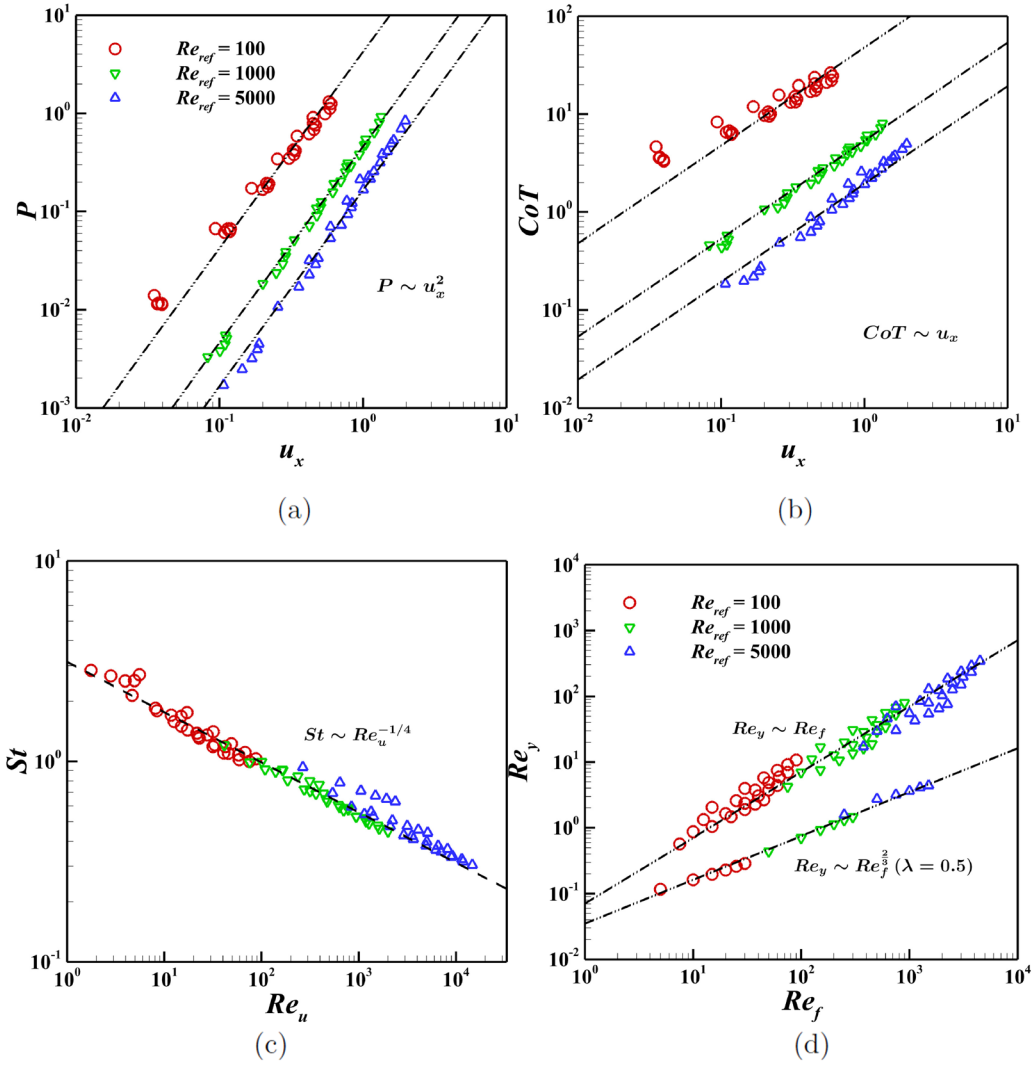

FIG. 12. The relationship between (a) the power consumption P and (b) the CoT and the propulsive speed. (c) The relationship between the St and the propulsive Reynolds number. (d) The relationship between the passive oscillating Reynolds number A_y and the flapping Reynolds number Re_f.

Published under an exclusive license by AIP Publishing

The passive oscillating Reynolds number (Re_y) based on the lateral oscillating amplitude of mass center is defined as $Re_y = f^* A_y \lambda^* / \nu$. It can be seen from Fig. 12(d) that the Re_y is highly linear with the Re_f and its relationship is related to the wavelength as follows:

$$\begin{cases} Re_y \sim Re_f^{2/3}, & \lambda = 0.5, \\ Re_y \sim Re_f, & \lambda > 0.5, \end{cases} \tag{10}$$

where the scaling law at $\lambda > 0.5$ is similar to the scaling law reported in Lin *et al.*[42] This finding is extremely valuable to AUVs designers for estimating the lateral oscillating amplitude to further reduce design cost and time.

V. CONCLUDING REMARKS

In summary, the present work investigates the hydrodynamic behaviors of an unconstrained carangiform swimmer with various undulatory frequencies and wavelengths at different Reynolds numbers.

Detailed investigation into the wavelength and undulatory frequency and the propulsive speed u_x revealed: the power consumption P and cost of transport are further enhanced with an increase in both wavelength and frequency. The time-averaged lateral speed u_y is close to zero and the passive oscillating amplitude A_y is closely related to the wavelength. The propulsive efficiency η largely depends on the undulatory frequency and the optimal wavelength to achieve high propulsive efficiency ranges from 0.75 and 1. The flow structures demonstrate that a large wavelength is beneficial for the amalgamation of the bound vortex, enhancing the strength of the shedding vortex. The amplitude of the tail-beat velocity only depends on the undulatory frequency, which explains why the swimmer with a high undulatory frequency can generate high-intensity wake vortices based on the same wavelength.

From the examination of Reynolds number effects, the propulsive speed u_x increases under similar conditions at high Re_{ref}, while the power consumption P and the cost of transport CoT decrease, inducing a higher propulsive efficiency due to the lower kinematic viscosity of the fluid environment at high Re_{ref} condition. In addition, the passive lateral oscillating amplitude A_y is reduced at high Re_{ref}, indicating that the viscous force is the dominant component of the lateral force and a small fluctuating lateral force is beneficial to stabilize the lateral passive oscillations. At $Re_{ref} = 100$, the boundary layer separates at the leading edge forming LEV and the shedding vortices are eliminated by the viscous dissipation failing to form rBvK configurations. At $Re_{ref} = 1000$ and 5000, the 2S-type rBvK vortex street is formed, generating the wake jet flow to provide the reactive thrust force.

This work echoes previous works[1] and reveals that the wavelength is a better representation of the characteristic length. The scaling law ($Re_u \sim Re_f^{4/3}$) is further improved with the use of wavelength, which is a more generalization parameter to evaluate propulsive performance of an unconstrained carangiform swimmer, especially at high Reynolds number condition ($Re_{ref} \geq 1000$). Based on the undulatory governing equation, the scaling relationship between Re_u and Re_f is proposed. In addition, the power consumption P, the cost of transport CoT, and the Strouhal number St satisfy the scaling relationships of $P \sim u_x^2$, CoT $\sim u_x$, and $St \sim Re_u^{-1/4}$, respectively. Moreover, the passive oscillating Reynolds number Re_y is found to satisfy some simple laws; when $\lambda = 0.5$, $Re_y \sim Re_f^{2/3}$; when $\lambda > 0.5$, $Re_y \sim Re_f$. The findings and the scaling law proposed in this work are crucial to design the next generation highly efficient AUVs. Note that the characteristics of vortex structures around a realistic swimmer might not be fully captured by the present 2D model. Therefore, other significant effects, such as the three-dimensional geometry and celerity, warrant further investigations.

ACKNOWLEDGMENTS

This work has been supported by the Key-Area Research and Development Program of Guangdong Province (No. 2021B0101190003), the Shenzhen Science & Technology Program (Grant No. KQTD20180411143441009), and the Department of Science and Technology of Guangdong Province (Grant Nos. 2019B21203001 and 2020B1212030001). Numerical simulations have been supported by the Center for Computational Science and Engineering of Southern University of Science and Technology.

AUTHOR DECLARATIONS

Conflict of Interest

The authors have no conflicts to disclose.

Author Contributions

Buchen Wu: Conceptualization (equal); Data curation (lead); Formal analysis (lead); Investigation (lead); Methodology (equal); Software (lead); Writing – original draft (lead). **Chang Shu:** Funding acquisition (equal); Methodology (equal); Software (equal); Supervision (equal); Writing – review & editing (equal). **Hsu Chew Lee:** Investigation (supporting); Writing – review & editing (supporting). **Minping Wan:** Conceptualization (equal); Funding acquisition (equal); Resources (equal); Supervision (equal); Writing – review & editing (equal).

DATA AVAILABILITY

The data that support the findings of this study are available within the article.

REFERENCES

[1] M. Gazzola, M. Argentina, and L. Mahadevan, "Scaling macroscopic aquatic locomotion," Nat. Phys. **10**, 758–761 (2014).
[2] M. S. Triantafyllou, G. Triantafyllou, and D. Yue, "Hydrodynamics of fishlike swimming," Annu. Rev. Fluid Mech. **32**, 33–53 (2000).
[3] I. Akhtar, R. Mittal, G. V. Lauder, and E. Drucker, "Hydrodynamics of a biologically inspired tandem flapping foil configuration," Theor. Comput. Fluid Dyn. **21**, 155–170 (2007).
[4] G. V. Lauder, "Fish locomotion: Recent advances and new directions," Annu. Rev. Mar. Sci. **7**, 521–545 (2015).
[5] G. Liu, Y. Ren, H. Dong, O. Akanyeti, J. C. Liao, and G. V. Lauder, "Computational analysis of vortex dynamics and performance enhancement due to body–fin and fin–fin interactions in fish-like locomotion," J. Fluid Mech. **829**, 65–88 (2017).
[6] M. S. U. Khalid, J. Wang, I. Akhtar, H. Dong, M. Liu, and A. Hemmati, "Why do anguilliform swimmers perform undulation with wavelengths shorter than their bodylengths?," Phys. Fluids **33**, 031911 (2021).
[7] L. Tian, Z. Zhao, W. Wang, and N. Liu, "Length and stiffness effects of the attached flexible plate on the flow over a traveling wavy foil," Acta Mech. Sin. **37**, 1404–1415 (2021).
[8] M. S. U. Khalid, J. Wang, H. Dong, and M. Liu, "Flow transitions and mapping for undulating swimmers," Phys. Rev. Fluids **5**, 063104 (2020).

Published under an exclusive license by AIP Publishing

[9]M. S. U. Khalid, J. Wang, I. Akhtar, H. Dong, M. Liu, and A. Hemmati, "Larger wavelengths suit hydrodynamics of carangiform swimmers," Phys. Rev. Fluids **6**, 073101 (2021).
[10]G. Li, I. Ashraf, B. François, D. Kolomenskiy, F. Lechenault, R. Godoy-Diana, and B. Thiria, "Burst-and-coast swimmers optimize gait by adapting unique intrinsic cycle," Commun. Biol. **4**, 40 (2021).
[11]M. Sfakiotakis, D. M. Lane, and J. B. C. Davies, "Review of fish swimming modes for aquatic locomotion," IEEE J. Oceanic Eng. **24**, 237–252 (1999).
[12]G. V. Lauder and P. G. Madden, "Learning from fish: Kinematics and experimental hydrodynamics for roboticists," Int. J. Autom. Comput. **3**, 325–335 (2006).
[13]J. Videler and C. Wardle, "Fish swimming stride by stride: Speed limits and endurance," Rev. Fish Biol. Fish. **1**, 23–40 (1991).
[14]W. M. Van Rees, M. Gazzola, and P. Koumoutsakos, "Optimal shapes for anguilliform swimmers at intermediate Reynolds numbers," J. Fluid Mech. **722**, R3 (2013).
[15]D. Zhang, G. Pan, L. Chao, and Y. Zhang, "Effects of Reynolds number and thickness on an undulatory self-propelled foil," Phys. Fluids **30**, 071902 (2018).
[16]J. Gray, "Studies in animal locomotion: VI. The propulsive powers of the dolphin," J. Exp. Biol. **13**, 192–199 (1936).
[17]G. I. Taylor, "Analysis of the swimming of long and narrow animals," Proc. R. Soc. London, Ser. A **214**, 158–183 (1952).
[18]M. Lighthill, "Note on the swimming of slender fish," J. Fluid Mech. **9**, 305–317 (1960).
[19]T. Y.-T. Wu, "Swimming of a waving plate," J. Fluid Mech. **10**, 321–344 (1961).
[20]J.-Y. Cheng, L.-X. Zhuang, and B.-G. Tong, "Analysis of swimming three-dimensional waving plates," J. Fluid Mech. **232**, 341–355 (1991).
[21]D. B. Quinn, G. V. Lauder, and A. J. Smits, "Scaling the propulsive performance of heaving flexible panels," J. Fluid Mech. **738**, 250–267 (2014).
[22]D. B. Quinn, K. W. Moored, P. A. Dewey, and A. J. Smits, "Unsteady propulsion near a solid boundary," J. Fluid Mech. **742**, 152–170 (2014).
[23]D. Floryan, T. Van Buren, and A. J. Smits, "Efficient cruising for swimming and flying animals is dictated by fluid drag," Proc. Natl. Acad. Sci. **115**, 8116–8118 (2018).
[24]Y.-L. Yu and K.-J. Huang, "Scaling law of fish undulatory propulsion," Phys. Fluids **33**, 061905 (2021).
[25]S. Gupta, A. Sharma, A. Agrawal, M. C. Thompson, and K. Hourigan, "Hydrodynamics of a fish-like body undulation mechanism: Scaling laws and regimes for vortex wake modes," Phys. Fluids **33**, 101904 (2021).
[26]B. J. Gemmell, S. P. Colin, J. H. Costello, and J. O. Dabiri, "Suction-based propulsion as a basis for efficient animal swimming," Nat. Commun. **6**, 8790 (2015).
[27]K. N. Lucas, G. V. Lauder, and E. D. Tytell, "Airfoil-like mechanics generate thrust on the anterior body of swimming fishes," Proc. Natl. Acad. Sci. **117**, 10585–10592 (2020).
[28]C.-Y. Guo, Y.-F. Kuai, Y. Han, P. Xu, Y.-W. Fan, and C.-D. Yu, "Hydrodynamic analysis of propulsion process of zebrafish," Phys. Fluids **34**, 021910 (2022).
[29]P. Han, G. V. Lauder, and H. Dong, "Hydrodynamics of median-fin interactions in fish-like locomotion: Effects of fin shape and movement," Phys. Fluids **32**, 011902 (2020).
[30]H. Liu, R. Wassersug, and K. Kawachi, "The three-dimensional hydrodynamics of tadpole locomotion," J. Exp. Biol. **200**, 2807–2819 (1997).
[31]M. Gazzola, W. M. Van Rees, and P. Koumoutsakos, "C-start: Optimal start of larval fish," J. Fluid Mech. **698**, 5–18 (2012).
[32]A. Zurman-Nasution, B. Ganapathisubramani, and G. Weymouth, "Influence of three-dimensionality on propulsive flapping," J. Fluid Mech. **886**, A25 (2020).
[33]J. Lu, H. Lei, C. Dai, L. Yang, and C. Shu, "Analyses and reconstruction of the lattice Boltzmann flux solver," J. Comput. Phys. **453**, 110923 (2022).
[34]X. Zhao, Z. Chen, L. Yang, N. Liu, and C. Shu, "Efficient boundary condition-enforced immersed boundary method for incompressible flows with moving boundaries," J. Comput. Phys. **441**, 110425 (2021).
[35]B. Wu, J. Lu, H. Lee, C. Shu, and M. Wan, "An efficient explicit immersed boundary-reconstructed lattice Boltzmann flux solver for isothermal fluid-structure interaction problems with large deformations and complex geometries," Appl. Math. Modell. **114**, 627–645 (2023).
[36]B. Wu, J. Lu, H. Lee, C. Shu, and M. Wan, "An explicit immersed boundary-reconstructed thermal lattice Boltzmann flux solver for thermal–fluid-structure interaction problems," Int. J. Mech. Sci. **235**, 107704 (2022).
[37]G.-J. Dong and X.-Y. Lu, "Characteristics of flow over traveling wavy foils in a side-by-side arrangement," Phys. Fluids **19**, 057107 (2007).
[38]P.-N. Sun, A. Colagrossi, and A.-M. Zhang, "Numerical simulation of the self-propulsive motion of a fishlike swimming foil using the δ^+-SPH model," Theor. Appl. Mech. Lett. **8**, 115–125 (2018).
[39]B. Wu, C. Shu, M. Wan, Y. Wang, and S. Chen, "Hydrodynamic performance of an unconstrained flapping swimmer with flexible fin: A numerical study," Phys. Fluids **34**, 011901 (2022).
[40]B. Wu, C. Shu, H. Lee, and M. Wan, "The effects of caudal fin's bending stiffness on a self-propelled carangiform swimmer," Phys. Fluids **34**, 041901 (2022).
[41]H. Liu, R. Wassersug, and K. Kawachi, "A computational fluid dynamics study of tadpole swimming," J. Exp. Biol. **199**, 1245–1260 (1996).
[42]X. Lin, J. Wu, and T. Zhang, "Self-directed propulsion of an unconstrained flapping swimmer at low Reynolds number: Hydrodynamic behaviour and scaling laws," J. Fluid Mech. **907**, R3 (2021).
[43]O. S. Pak and E. Lauga, "The transient swimming of a waving sheet," Proc. R. Soc. A **466**, 107–126 (2010).
[44]N. T. Jafferis, H. A. Stone, and J. C. Sturm, "Traveling wave-induced aerodynamic propulsive forces using piezoelectrically deformed substrates," Appl. Phys. Lett. **99**, 114102 (2011).
[45]F.-B. Tian, X.-Y. Lu, and H. Luo, "Propulsive performance of a body with a traveling-wave surface," Phys. Rev. E **86**, 016304 (2012).

Published under an exclusive license by AIP Publishing